

# Sub-Rayleigh Imaging via $N$ -Photon Detection

Fabrizio Guerrieri<sup>1,2</sup>, Lorenzo Maccone<sup>2</sup>, Franco N. C. Wong<sup>2</sup>, Jeffrey H. Shapiro<sup>2</sup>, Simone Tisa<sup>3</sup>, and Franco Zappa<sup>1</sup>

<sup>1</sup>*Politecnico di Milano, Dipartimento di Elettronica e Informazione, 20133 Milano, Italy*

<sup>2</sup>*Research Laboratory of Electronics, Massachusetts Institute of Technology, Cambridge, Massachusetts 02139, USA*

<sup>3</sup>*Micro Photon Devices, via Stradivari 4, 39100 Bolzano, Italy*

The Rayleigh diffraction bound sets the minimum separation for two point objects to be distinguishable in a conventional imaging system. We demonstrate resolution enhancement beyond the Rayleigh bound using random scanning of a highly-focused beam and  $N$ -photon photodetection implemented with a single-photon avalanche detector array. Experimental results show resolution improvement by a factor  $\sim\sqrt{N}$  beyond the Rayleigh bound, in good agreement with theory.

PACS numbers: 42.50.-p, 42.50.Ar, 42.79.Pw, 42.30.Va

The response of a diffraction-limited imaging system to a point-like source—its point spread function (PSF)—has extent inversely proportional to the entrance pupil's area. The image is obtained by convolving the system PSF with the light distribution of the object. Therefore, details finer than the PSF's extent are lost under conventional (entire-object) illumination. The Rayleigh diffraction bound sets the minimum separation for two object points to be distinguishable in the image.

Two classes of quantum strategies have been suggested to circumvent this bound. The first relies on techniques from quantum metrology [1], in which the image information is encoded into suitably tailored non-classical light beams [2–4]. For example, quantum lithography [5] exploits the effective de Broglie wave-function of  $N$  photons in a delicately crafted state to obtain an increase in resolution proportional to  $N$  (see [6] for recent developments). These methods are typically extremely sensitive to photon loss and noise, because they rely on delicate quantum effects (such as squeezing and entanglement). Thus they are best suited to short-distance applications, such as microscopy, where losses can be controlled, as opposed to standoff sensing, such as laser radar operation over km or longer path lengths, for which substantial diffraction and atmospheric losses will be present.

The second class of quantum strategies for beating the Rayleigh diffraction bound exploit postselection [7] to extract the high-resolution image associated with a non-classical component from classical-state light containing information about the object to be imaged [8–17]. Because postselection involves discarding part of the measurement data, these procedures inherently suffer detection inefficiency that increases the time required to acquire an image. However, their spatial resolution can nonetheless exceed the Rayleigh diffraction bound. Furthermore, because they employ classical-state (laser) light, these techniques degrade gracefully with increasing loss and noise, making them suitable for standoff sensing. In this Letter we report the first experimental demonstration of one such technique, viz., that of Giovannetti *et al.* [17], in which the object is illuminated by a focused light source and scanned. The scanning pattern is irrelevant

so long as the area of interest is covered, i.e., a random scan pattern suffices. The image is formed using only those pixels that count exactly  $N$  photons within a measurement time  $T$ . The expected resolution improvement is  $\sqrt{N}$  over standard entire-object illumination, until the limit set by the focused-beam illumination. We begin with the theory for this technique.

*Theory:*— We are interested in an active imager, such as a laser radar, comprised of a transmitter and a receiver in which we control the object illumination and form the image with the receiver. For such systems, the spatial resolution is a function of two antenna patterns, viz., the transmitter's illumination pattern on the object *and* the receiver antenna pattern, set by the diffraction limit of its optics, projected onto the object. When floodlight illumination is employed, so that the entire object is bathed in light, the resolution limit is set by the receiver's Rayleigh diffraction bound. If the transmitter and receiver are co-located, they can share the same optics so that their antenna patterns have identical Rayleigh bounds whose product gives the overall resolution behavior. Alternatively, if a small transmitter is located much closer to the object than is the receiver, it is possible to project very small spots onto the object to be imaged. If this is done in a precision scan, so that the receiver knows exactly where the transmitter is pointing at any instant in time, a simple energy measurement at the receiver will realize resolution limited by the transmitter's antenna pattern, regardless of the receiver's own Rayleigh bound. However, creating that precision scan, and relaying the scan positions to the receiver, could easily be a major challenge, especially if the transmitter is mounted on a small unmanned air vehicle. The postselection technique of Giovannetti *et al.* circumvents that problem by allowing the scan pattern to be arbitrary, even random, so long as the object's region of interest is covered.

Suppose that a focused transmitter emits a  $+z$ -going, quasimonochromatic, paraxial, linearly-polarized laser pulse with scalar complex envelope  $E_T(\boldsymbol{\rho}, t; \boldsymbol{\theta}) = \sqrt{4N_T/\pi D_T^2} s(t) e^{-ik|\boldsymbol{\rho}|^2/2L_T + ik\boldsymbol{\theta}\cdot\boldsymbol{\rho}}$  for  $|\boldsymbol{\rho}| \leq D_T/2$ , where  $\boldsymbol{\rho} = (x, y)$  is the transverse coordinate vector,  $\boldsymbol{\theta} = (\theta_x, \theta_y)$  is the transmitter aim angle, and  $k$  is the wave

number at the center wavelength  $\lambda$ . We will normalize  $E_T$  to have units  $\sqrt{\text{photons}/\text{m}^2\text{s}}$ , and take the pulse shape  $s(t)$  to satisfy  $\int dt |s(t)|^2 = 1$ , so that  $N_T$  is the average transmitted photon number [18]. This pulse transilluminates an object  $L_T$ -m away from the transmitter [19]. The light that passes through the object is then collected by a diffraction-limited circular lens of diameter  $D_R$  located  $L_R$ -m in front of the object. The focal length of this lens is such that it casts an image of the object at a distance  $L_I > L_R$  beyond the lens. Neglecting the propagation delay and correcting for image inversion, the photon-flux density in the image plane is then

$$|E_{\text{IM}}(\boldsymbol{\rho}_{\text{IM}}, t; \boldsymbol{\theta})|^2 = N_T |s(t)|^2 \times \left| \int d\boldsymbol{\rho} \mathcal{O}(\boldsymbol{\rho}) \sqrt{\frac{\pi D_T^2}{4(\lambda L_T)^2} \frac{\pi D_R^2}{4\lambda^2 L_R L_I}} e^{ik|\boldsymbol{\rho}|^2(L_T^{-1} + L_R^{-1})/2} \times \frac{J_1(\pi D_T |\boldsymbol{\rho} - \boldsymbol{\theta}_{L_T}|/\lambda L_T)}{\pi D_T |\boldsymbol{\rho} - \boldsymbol{\theta}_{L_T}|/2\lambda L_T} \frac{J_1(\pi D_R |\boldsymbol{\rho} - \boldsymbol{\rho}_{\text{IM}}/m|/\lambda L_R)}{\pi D_R |\boldsymbol{\rho} - \boldsymbol{\rho}_{\text{IM}}/m|/2\lambda L_R} \right|^2,$$

where  $\mathcal{O}(\boldsymbol{\rho})$  is the object's field-transmission function,  $m \equiv L_I/L_R$  is the image magnification [20], and we see the transmitter and receiver's circular-pupil antenna patterns.

To exhibit the sub-Rayleigh resolution capability of the scheme from [17] we shall assume that: (1) the transmitter's antenna pattern fully resolves all significant features in  $\mathcal{O}(\boldsymbol{\rho})$  [21]; (2) the image-plane photon counting array has pixels of area  $A_p$  sufficiently small that diffraction, rather than pixel size, limits image resolution; and (3) the photon counting array outputs pixel counts taken over the full  $T$ -s-long extent of  $s(t)$ . For a given illumination angle  $\boldsymbol{\theta}$ , the pixel counts are then statistically independent, Poisson random variables with mean value, for the pixel centered at  $\boldsymbol{\rho}_{\text{IM}}$ , given by

$$\bar{N}_{\boldsymbol{\theta}}(\boldsymbol{\rho}_{\text{IM}}) = \eta N_T |\mathcal{O}(\boldsymbol{\theta}_{L_T})|^2 \frac{\pi D_R^4 L_T^2 A_p}{4 D_T^2 \lambda^2 L_R^2 L_I^2} \times \left( \frac{J_1(\pi D_R |\boldsymbol{\theta}_{L_T} - \boldsymbol{\rho}_{\text{IM}}/m|/\lambda L_R)}{\pi D_R |\boldsymbol{\theta}_{L_T} - \boldsymbol{\rho}_{\text{IM}}/m|/2\lambda L_R} \right)^2,$$

where  $\eta$  is the detector's quantum efficiency. If photon counts are collected from the pixel at  $\boldsymbol{\rho}_{\text{IM}}$  while  $\boldsymbol{\theta}$  is randomly scanned over the object region, the unconditional probability of getting  $N$  counts from that pixel is

$$P_N(\boldsymbol{\rho}_{\text{IM}}) = \int d\boldsymbol{\theta} p(\boldsymbol{\theta}) \frac{\bar{N}_{\boldsymbol{\theta}}(\boldsymbol{\rho}_{\text{IM}})^N e^{-\bar{N}_{\boldsymbol{\theta}}(\boldsymbol{\rho}_{\text{IM}})}}{N!},$$

where  $p(\boldsymbol{\theta})$  is the scan pattern's probability density function. Postselecting those pixels for which  $N$  counts have been registered, we get an image  $\mathcal{I}_N(\boldsymbol{\rho}_{\text{IM}}) \propto P_N(\boldsymbol{\rho}_{\text{IM}})$ . For  $N > \max \bar{N}_{\boldsymbol{\theta}}(\boldsymbol{\rho}_{\text{IM}})$ , the Poisson distribution is monotonically decreasing with increasing  $N$ , whence

$$\mathcal{I}_N(\boldsymbol{\rho}_{\text{IM}}) \sim \int d\boldsymbol{\theta} p(\boldsymbol{\theta}) |\mathcal{O}(\boldsymbol{\theta}_{L_T})|^{2N} \times \left( \frac{J_1(\pi D_R |\boldsymbol{\theta}_{L_T} - \boldsymbol{\rho}_{\text{IM}}/m|/\lambda L_R)}{\pi D_R |\boldsymbol{\theta}_{L_T} - \boldsymbol{\rho}_{\text{IM}}/m|/2\lambda L_R} \right)^{2N},$$

where we have suppressed multiplicative constants and ignored the exponential term as it is independent of  $N$ . Here we see that the postselected image contains  $|\mathcal{O}|^{2N}$  convolved with the  $N$ th power of the receiver's Airy disk pattern, i.e., a point-spread function that is  $\sim\sqrt{N}$  narrower than the Airy disk itself when compared on a main-lobe area basis [17]. Note that violating the preceding monotonicity condition can lead to the "donut-hole" effect exhibited in the experiments described below.

*Experiment:*— We demonstrate the concept of sub-Rayleigh imaging with the setup shown in Fig. 1(a). The object to be imaged in transmission was part of a U.S. Air Force (USAF) resolution target consisting of alternate opaque and clear stripes of width  $125 \mu\text{m}$  (4 line pairs/mm), as indicated by the arrow in Fig. 2(a). A 532-nm laser was mounted on an  $XY$  translation stage that provided scan coverage over the entire object with a 20- $\mu\text{m}$ -radius focused spot. We imaged the object through a  $f = 25$ -cm diffraction-limited lens set in a 2-mm-diameter aperture. The optics provided  $5.3\times$  image magnification, yielding a 660- $\mu\text{m}$ -wide strip at the image plane. Under conventional (entire-object) illumination, shown in the setup of Fig. 1(b), the Rayleigh diffraction bound for the imaging system at the image plane was 1.86 mm, which is  $\sim 2.8\times$  larger than the stripe width. Figure 2(b) shows the conventional-illumination image that was obtained using standard photodetection (with all events counted): the stripes are unresolved, as expected. Note that with full illumination of the object, we were not able to go beyond the Rayleigh bound even with the  $N$ -photon detection scheme, indicating that focused illumination is a necessary requirement.

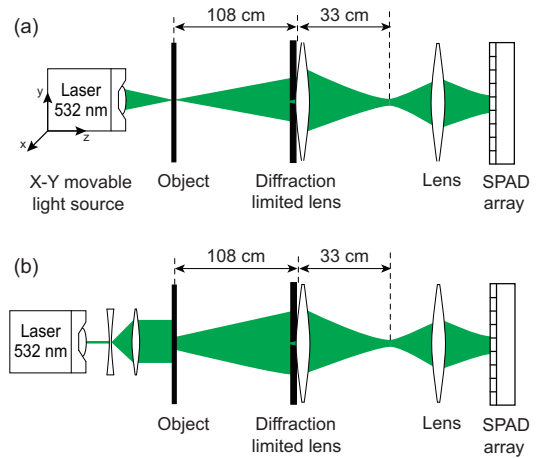


FIG. 1: (color online). Setup schematics for (a) sub-Rayleigh imaging with focused illumination, and (b) conventional coherent imaging with full illumination.

The detector was a compact  $32 \times 32$  Si single-photon avalanche diode (SPAD) array fabricated with a complementary metal oxide semiconductor (CMOS) process [22]. The Si SPAD was a  $p$ - $n$  junction reverse-biased

above its breakdown voltage and operated in the Geiger mode with a detection efficiency of  $\sim 30\%$  at 532 nm. Each pixel of the CMOS SPAD array consisted of one SPAD with its front-end active quenching and resetting electronics and a digital counting circuitry for in-pixel pre-processing. The pixel pitch for the array was  $100\ \mu\text{m}$ , and the SPAD had a fill factor of only 3.1% at each pixel due to the presence of on-chip electronics. Owing to the large separation between SPADs we did not observe any cross talk. The average pixel dead time (including all the electronic circuitry) was 300 ns. Each SPAD delivered a digital output pulse for every single-photon detection event with no readout noise. The in-pixel counting circuitry would compute the number of single-photon events within its user-selectable integration time of  $1\ \mu\text{s}$  or more and store the tally in an in-pixel memory cell. By measuring incident photons over a long integration time,  $N$ -photon sensitivity in the time domain can be achieved at the single-pixel level. The array readout was performed through an 8-bit data bus without interrupting the next 1024-pixel frame of photon-counting integration, and the maximum frame rate was  $10^5/\text{s}$ . A typical integration time of each frame was tens of  $\mu\text{s}$ .

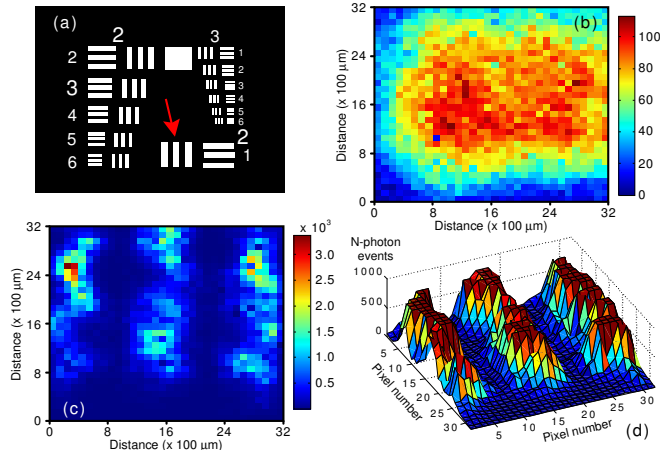


FIG. 2: (color online). (a) Object indicated by arrow: target #1, group 2 of a USAF resolution target, composed of opaque and clear stripes  $125\ \mu\text{m}$  wide. (b) Blurred image obtained conventionally using full illumination and taken in a single  $50\text{-}\mu\text{s}$  frame; Rayleigh diffraction bound is  $1.86\ \text{mm}$ . (c) Sub-Rayleigh image using focused illumination and  $N = 23$ . Details are obscured by a few pixels with very high event counts. (d) 3-D intensity profile of (c) with the stripes clearly revealed by clipping pixels with very high event counts at the limit of 800.

To implement sub-Rayleigh imaging in Fig. 1(a) we manually scanned the focused beam in a random pattern, making sure that there was coverage for the entire area of interest. At each scan location, we recorded over 8000 measurement frames for image averaging that took less than 1 second to accomplish. The incident power was adjusted to have an average peak photocount  $\bar{N}_{\text{peak}} = 14$

per integration time (for one pixel). For each measurement frame, each pixel with exactly  $N$  photocounts (after dark-count subtraction, measured separately) was tagged as having an  $N$ -photon event. All other pixels were then tagged for zero  $N$ -photon events. The measurement process was then repeated at a different scan location until the object of interest was fully scanned. Figure 2(c) shows the resultant image for  $N = 23$ , revealing the three stripes that were lost under conventional illumination in Fig. 2(b). The color scale of Fig. 2(c) has a large range to accommodate several pixels with very high event counts and therefore image details (with lower event frequencies) are obscured. Figure 2(d) shows the 3-D intensity profile of the same  $N = 23$  image of Fig. 2(c), except that we cap the event occurrence at 800 for pixels with over 800 events in order to make the lower-count pixels more visible, thus revealing the three stripes very clearly. According to theory, the expected enhancement of  $\sqrt{N}$  should yield a sub-Rayleigh resolution of  $\sim 1.86/\sqrt{23} = 0.4\ \text{mm}$  is qualitatively borne out by our results. Note that the sub-Rayleigh resolution still exceeds the  $106\text{-}\mu\text{m}$ -limit set (after magnification) by the focused illumination at the object, as expected.

We chose  $N = 23$  to be substantially larger than  $\bar{N}_{\text{peak}} = 14$  to avoid the “donut-hole” problem. To illustrate this issue, Fig. 3 shows images of a point source obtained under various measurement conditions. The aperture diameter of the imaging optics in Fig. 1(a) was set to  $3\ \text{mm}$  with the same overall image magnification of 5.3 so that the Rayleigh bound at the image plane (SPAD array) was  $1.2\ \text{mm}$ . We removed the USAF resolution target so that the  $20\text{-}\mu\text{m}$ -radius focused spot at the object plane served as the point source, and no scanning was necessary for these images. We took  $\sim 32,000$  measurement frames, recorded the photocounts at each pixel for each frame, binned them accordingly after subtracting dark counts, and processed the data. Figure 3(a) shows the cross section of the Rayleigh-bound image of the point source through the 3-mm-diameter aperture obtained by including all photocounts to yield an intensity profile averaged over the  $\sim 32,000$  frames. We measured  $\bar{N}_{\text{peak}} \approx 15$  and, as an indicator for the image size, we obtained the full-width at half-maximum (FWHM) of  $\sim 1\ \text{mm}$ .

Figures 3(b)–(d) are cross-sectional profiles obtained by selecting exactly  $N$ -photocounts for  $N = 9, 15,$  and  $23$ , that are respectively smaller than, equal to, and greater than  $\bar{N}_{\text{peak}}$ . For  $N < \bar{N}_{\text{peak}}$  in (b), the center portion of the point-source image usually received more than the threshold level  $N$  and therefore had few exactly  $N$ -photon events. On the other hand, the photocounts away from the center decrease from  $\bar{N}_{\text{peak}}$  until the photocount average matches the threshold  $N$  where it shows a peak, and hence the image has a “donut-hole” shape [23]. For  $N \approx \bar{N}_{\text{peak}}$  in (c), the profile is single-peaked and looks slightly narrower and steeper than the Rayleigh-bound image in Fig. 3(a) which is much larger than the mag-

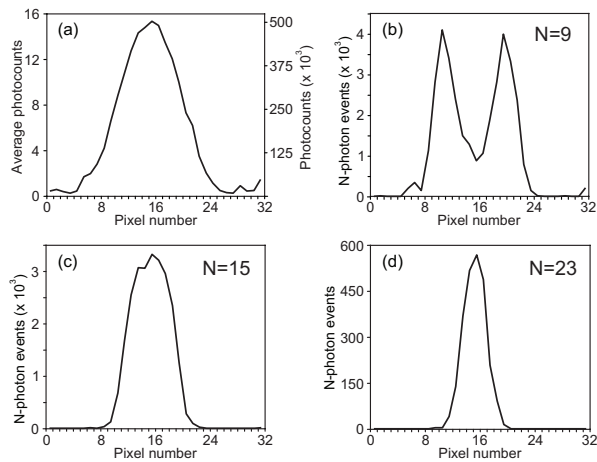


FIG. 3: Image cross section of a point source with a modified setup of Fig. 1(a) (3-mm aperture) obtained by collecting: (a) all photocounts as in conventional imaging with  $\bar{N}_{\text{peak}} \approx 15$ ; (b) exactly  $N = 9$  photocounts and showing a hole where a peak should be, (c) exactly  $N = 15$  photocounts with a peak slightly sharper than in (a); and (d) exactly  $N = 23$  photocounts with a sub-Rayleigh peak that is sharper than (c).

nified size of the focused beam of  $125 \mu\text{m}$  (FWHM) at the image plane. When  $N \gg \bar{N}_{\text{peak}}$ , as required for sub-Rayleigh imaging, we observe in (d) that the profile for  $N = 23$  shows a much narrower peak with a FWHM width of  $\sim 0.4 \text{ mm}$  that is smaller than the 1-mm width (FWHM) of the Rayleigh-bound point source image in Fig. 3(a). We also note that the  $N = 23$  event frequency is much lower than for  $N$  less than or equal to  $\bar{N}_{\text{peak}}$ , because such a large  $N$  did not happen very often. Our sub-Rayleigh imaging has characteristics that are similar to  $N$ -photon interferometry, in which sub-wavelength ( $\lambda/N$ ) interference patterns were obtained with coherent-state input and postselective  $N$ -photon detection [24].

Our point-source images suggest the following physical origin for the formation of the Rayleigh diffraction bound and the basis for our sub-Rayleigh imaging technique. The donut holes that form for  $N < \bar{N}_{\text{peak}}$  are responsible for the diffractive spread of the imaging system. By removing the low- $N$  photocount events and those comparable to  $\bar{N}_{\text{peak}}$ , one captures the much narrower profile for  $N \gg \bar{N}_{\text{peak}}$  at the expense of longer acquisition times due to less frequent occurrences for high values of  $N$ . We should also achieve similar results if we relax the measurement requirement from exactly  $N$  for  $N \gg \bar{N}_{\text{peak}}$  to a sum of all  $N \gg \bar{N}_{\text{peak}}$ , whose resolution should be dominated by its lowest  $N$  term due to its larger sub-Rayleigh width ( $\propto 1/\sqrt{N}$ ) and higher rate of occurrence.

In conclusion, we have demonstrated sub-Rayleigh imaging resolution using a classical light source, tight focusing on the object, and  $N$ -photon photodetection. The sub-Rayleigh technique removes the low- $N$  image components that contribute to the diffractive spread of the imaging system. The measured resolution enhancement

of  $\sim \sqrt{N}$  is in good agreement with theory. The sub-Rayleigh technique may find applications in which active illumination can be implemented to obtain a higher resolution image at the expense of longer acquisition times.

We thank J. Le Gouët for help with the experiment. F. G. acknowledges the Roberto Rocca Doctoral Fellowship. This work was supported in part by the W. M. Keck Foundation Center for Extreme Quantum Information Theory, the U.S. Army Research Office under a Multi-disciplinary University Research Initiative grant, and the DARPA Quantum Sensors Program.

- 
- [1] V. Giovannetti, S. Lloyd, and L. Maccone, *Science* **306**, 1330 (2004); *Phys. Rev. Lett.* **96**, 010401 (2006); S. L. Braunstein, *Nature* **440**, 617 (2006).
  - [2] See, e.g., M. I. Kolobov, *Rev. Mod. Phys.* **71**, 1539 (1999); M. I. Kolobov (Ed.) *Quantum Imaging*, (Springer, New York, 2006).
  - [3] Y. Shih, *IEEE J. Sel. Topics in Quantum Electron.* **13**, 1016 (2007).
  - [4] L.A. Lugiato *et al.* *J. Opt. B* **4**, S176 (2002).
  - [5] A. N. Boto, *et al.*, *Phys. Rev. Lett.* **85**, 2733 (2000).
  - [6] M. Tsang, *Phys. Rev. Lett.* **102**, 253601 (2009).
  - [7] K. L. Pagnell and D. T. Pegg, *J. Mod. Opt.* **51**, 1613 (2004).
  - [8] P. R. Hemmer, *et al.*, *Phys. Rev. Lett.* **96**, 163603 (2006); A. Muthukrishnan, M. O. Scully, and M. S. Zubairy, *J. Opt. B: Quantum Semiclass. Opt.* **6**, S575 (2004).
  - [9] C. Thiel *et al.*, *Phys. Rev. Lett.* **99**, 133603 (2007).
  - [10] S. J. Bentley and R. W. Boyd, *Opt. Exp.* **12**, 5735 (2004).
  - [11] M. Zhang *et al.*, *Phys. Lett. A* **366**, 569 (2007).
  - [12] K. Wang and D.-Z. Cao, *Phys. Rev. A* **70**, 041801(R) (2004).
  - [13] D. Korobkin and E. Yablonovitch, *Opt. Eng.* **41**, 1729 (2002).
  - [14] E. Yablonovitch and R. B. Vrijen, *Opt. Eng.* **38**, 334 (1999).
  - [15] A. Pe'er *et al.*, *Opt. Express* **12**, 6600 (2004).
  - [16] B. I. Erkmen and J. H. Shapiro, *Phys. Rev. A* **77**, 043809 (2008).
  - [17] V. Giovannetti, S. Lloyd, L. Maccone, J. H. Shapiro, *Phys. Rev. A* **79**, 013827 (2009).
  - [18] Without loss of generality, we use semiclassical photodetection theory in what follows, hence a classical field description suffices, see, e.g., J. H. Shapiro, *IEEE J. Sel. Topics in Quantum Electron.* **15**, 1547 (2009).
  - [19] Standoff sensing is ordinarily done in reflection, but we assume transillumination here to match our experiment.
  - [20] Laser radar operation would employ  $L_I < L_R$ , hence image minification. We have specified  $L_I > L_R$  to match our experiment.
  - [21] If  $d$  is the minimum size of any significant  $\mathcal{O}(\rho)$  feature, then we require  $dD_T/\lambda L_T \gg 1$ .
  - [22] F. Guerrieri, S. Tisa, A. Tosi, and F. Zappa, *Proc. SPIE* **7536**, 753605 (2010).
  - [23] A. J. Pearlman, *et al.*, *Opt. Express* **18**, 6033 (2010).
  - [24] G. Khoury, H. S. Eisenberg, E. J. S. Fonseca, and D. Bouwmeester, *Phys. Rev. Lett.* **96**, 203601 (2006).